Materials Today Bio 23 (2023) 100848

Contents lists available at ScienceDirect

Materials Today Bio

journal homepage: www.journals.elsevier.com/materials-today-bio

Construction of multifunctional coating with cationic amino acid-coupled peptides for osseointegration of implants

Bingyang Zhao [a,1], Yilong Dong [b,1], Xinkun Shen [b], Wei He [a], Hairu Jin [a], Lili yao [a], Sheng wu Zheng [c], Xingjie Zan [d,**], Jiming Liu [a,*]

[a] School & Hospital of Stomatology, Wenzhou Medical University, Wenzhou, 325035, China
[b] Department of Orthopaedics, The Third Affiliated Hospital of Wenzhou Medical University (Ruian People's Hospital), Wenzhou, 325016, China
[c] Wenzhou Celecare Medical Instruments Co.,Ltd, Wenzhou, 325000, China
[d] Wenzhou Key Laboratory of Perioperative Medicine, Wenzhou Institute, University of Chinese Academy of Sciences, Wenzhou, 325000, China

ARTICLE INFO

Keywords:
Polypeptide
Multifunctional coating
Tannic acid
Layer-by-layer assembly
Implant osseointegration

ABSTRACT

Osseointegration is an important indicator of implant success. This process can be improved by coating modified bioactive molecules with multiple functions on the surface of implants. Herein, a simple multifunctional coating that could effectively improve osseointegration was prepared through layer-by-layer self-assembly of cationic amino acids and tannic acid (TA), a negatively charged molecule. Osteogenic growth peptide (OGP) and the arginine-glycine-aspartic acid (RGD) functional polypeptides were coupled with Lys_6 (K_6), the two polypeptides then self-assembled with TA layer by layer to form a composite film, (TA-OGP@RGD)n. The surface morphology and biomechanical properties of the coating were analyzed in gas and liquid phases, and the deposition process and kinetics of the two peptides onto TA were monitored using a quartz crystal microbalance. In addition, the feeding consistency and adsorption ratios of the two peptides were explored by using fluorescence visualization and quantification. The (TA-OGP@RGD)n composite membrane mediated the early migration and adhesion of cells and significantly promoted osteogenic differentiation and mineralization of the extracellular matrix in vitro. Additionally, the bifunctional peptide exhibited excellent osteogenesis and osseointegration owing to the synergistic effect of the OGP and RGD peptides in vivo. Simultaneously, the (TA-OGP@RGD)n membrane regulated the balance of reactive oxygen species in the cell growth environment, thereby influencing the complex biological process of osseointegration. Thus, the results of this study provide a novel perspective for constructing multifunctional coatings for implants and has considerable application potential in orthopedics and dentistry.

1. Introduction

The integration of implant and bone tissue called osseointegration, after implantation is a complex process that involves various cells and biomolecules. This includes process such as cell adhesion, cell migration, osteogenic differentiation, and extracellular matrix (ECM) mineralization, which are crucial to the success of osseointegration [1–4]. Rapid cell adhesion and migration enable cells to occupy the interface between the implant and bone tissue, this not only reduces the risk of bacterial infection but also provides a basis for cell osteogenic differentiation and mineralization [5]. Programmed osteogenic differentiation and ECM mineralization can promote bone formation and remodeling, which is the key for successful osseointegration [6]. In addition, reactive oxygen species (ROS) regulate cell behavior through redox signals to maintain homeostasis in the bone tissue environment. Foreign body implantation and trauma fragments induce excessive ROS production in the area around the implant, which negatively affects osseointegration [7,8]. For example, excessive ROS levels can reduce the rate of cell adhesion and migration, promote bone resorption, and inhibit osteogenesis. Therefore, the importance of maintaining normal ROS levels in the bone tissue environment to enable osteogenesis cannot be overlooked [9,10]. Accumulating evidence has shown that preparing implants with multiple bioactive functions can aid in the above complex biological processes and overcome the associated challenges to promote

* Corresponding author.
** Corresponding author.
E-mail addresses: zanxj@ucas.ac.cn (X. Zan), sdplljm@126.com (J. Liu).
[1] These authors contributed equally to this work.

https://doi.org/10.1016/j.mtbio.2023.100848
Received 18 August 2023; Received in revised form 22 October 2023; Accepted 26 October 2023
Available online 28 October 2023

osseointegration.

Functional peptides derived from living organisms can confer material surfaces with activity and regulate cell behavior. Compared with proteins, these peptides have the advantages of having a simple structure, high activity, and strong specificity [11–13]. With the gradual advancement and cost reduction of peptide synthesis technology, numerous biologically active peptides have been applied in bone tissue engineering [14]. For example, the arginine-glycine-aspartic acid (RGD) sequence extracted from ECM proteins can specifically bind to 11 types of integrins on cell membranes and has been widely modified for use on implant surfaces to improve cell adhesion and migration [15]. Osteogenic growth peptide (OGP) is a physiologically endogenous 14-residue peptide present in human serum and is widely used in bone tissue engineering for its ability to promote the proliferation and differentiation of osteoblasts and bone marrow stem cells [16,17]. BFP-1, a derivative peptide of bone morphogenetic protein-7 (BMP-7), exhibits angiogenic properties and can significantly promote bone formation [18]. Thus, integrating peptides with different functions at the material interface to develop multifunctional implants is an effective strategy to achieve implant–bone integration.

Previous studies have used a wide range of methods to integrate peptides and construct multifunctional implants with surface coating. Mas-Moruno et al. constructed a novel peptide–based platform for the dual expression of bioactive peptides using solid-phase synthesis [19] with the help of Lys active residues to connect two active sequences, i.e., RGD adhesion polypeptide and lactoferrin-derivatized LF1-11 antimicrobial peptides. Thereafter, the platform was grafted onto the surface of titanium by introducing sulfhydryl groups to develop an adhesion-promoting and antibacterial multifunctional surface [20]. However, this synthetic method majorly relies on thiol-metal interface interactions and is not a universal immobilization method. Fusion peptides can simultaneously exhibit various biological behaviors that can effectively solve the problem of limited fixed sites. Wang et al. synthesized fusion peptides using the orthogonal click technology to promote Cu(I)-catalyzed azidoalkyl cycloaddition (CuAAC-sb) through the sodium borohydride reduction to immobilize HHC36 antibacterial sequences and QK angiogenic sequences [21]. Subsequently, a multifunctional implant coating exhibiting both vascularization and antibacterial properties was developed using the click reaction on the surface of titanium and an alkyne-containing alkane coupling agent, thus effectively promoting osseointegration. However, excessively long fusion peptide chains may cause lead to structural changes occurring in the amino acid sequence, such as dislocation or loss. Furthermore, the original conformation becomes difficult to maintain because of similar polypeptide domains, which can affect the function. Moreover, the synthesis and purification of fusion peptides is both time and resource-consuming and easily affected by environmental factors (e.g., temperature and pH). This can lead to problems with stability and consistency that limit clinical application. Some studies have simply blended two different peptides while effectively controlling their ratio; however, the presentation of peptide groups at the material interface remains elusive [22–24]. Although substantial progress has been made in the construction of multifunctional implant interface because of these reports, overcoming these challenges and improving the efficiency and reliability of peptide-modified materials remains considerably challenging. Therefore, novel methods and techniques are being explored.

Layer-by-layer (LbL) self-assembly is a simple, efficient, and universal surface-modification technology. Traditional LbL assembly units usually involve polymers [25]. The polymer structure can be complex; active biomolecules can be easily buried under the modified layer and may not be sensed by receptors on the cell membrane. Tannic acid (TA) is a natural polyphenol derived from plant sources and is rich in phenolic hydroxyl groups. It provides abundant reactive sites and can serve as a versatile platform for material engineering and surface functionalization. Moreover, TA is rich in catechol groups, which exhibit strong affinity for various substrates and can actively inhibit microbial adhesion and colonization [26,27], and play a crucial role in bone tissue engineering. In a previous study on the supramolecular assembly of peptides [28], we found that polyphenols exhibit multiple synergistic cross-linking interactions with different peptide side groups and that in the interaction ratio between positively charged peptides and polyphenols in the peptide-polyphenol network, other amino acids are stronger. The ability of polyphenols to readily complex with different types of polypeptides can lead to the development of various functional materials for various applications.

Therefore, in the present study, we redesigned the OGP and the RGD polypeptides (OGP/RGD) and connected these to the cationic amino acid sequence Lys_6 at the front end (Scheme 1a and b) to ensure that they can self-assemble with TA in a simple LbL manner by virtue of the interaction force of the polypeptide-polyphenol network, thereby obtaining a multifunctional implant coating to promote osteointegration (Scheme 1c). Our results show that the (TA-OGP@RGD)n membrane is an effective multifunctional coating material that can effectively promote early cell migration and adhesion during osseointegration and regulate ROS and inducing early differentiation and mineralization of osteoblasts, which is a novel and effective strategy to improve implant osseointegration. We believe that this strategy will provide as a basis for the construction of an efficient multifunctional implant interface in the future.

2. Experimental section

2.1. Materials

TA (molecular weight, 1701.2 Da), OGP (KKKKKK-GGYGFGG-YGFGG), and RGD cell adhesion (KKKKKK-Acp-RGD-Acp-RGD-Acp-RGD) polypeptides were synthesized by Hangzhou Specialized Peptide Biology Co. Ltd (Hangzhou, China). Polyethyleneimine (PEI; 10,000 99 %), 30 % hydrogen peroxide (H_2O_2), 25 % ammonia, 98 % sulfuric acid, tris(hydroxymethyl)-aminomethane (Tris) (≥99 %), and 4,6-diamidino-2-phenylindole (DAPI) were purchased from Sigma. Paraformaldehyde (4 %), Triton X-100, sodium β-glycerophosphate, alizarin red S, and fetal bovine serum (FBS) were purchased from Solarbio Life Science. Vitamin C, BCIP/NBT alkaline phosphatase kit, Cell Counting Kit-8 (CCK-8), and ferric reducing antioxidant power (FRAP) assay kits were purchased from Beyotime Institute of Biotechnology. Silicon wafers and 14-mm-diameter round glass coverslips were washed at 98 °C with piranha solution (30 % hydrogen peroxide and 70 % concentrated sulfuric acid, V/V) for 2 h, followed by repeated washing with anhydrous ethanol and deionized water under sonication, and dried under nitrogen airflow.

2.2. Preparation of the(TA-RGD)n, (TA-OGP)n, and (TA-RGD@OGP)n coating

Tannic acid (1 mg/mL), RGD (1 mg/mL), OGP (1 mg/mL) and RGD@OGP (1:1, c1/c2, 1 mg/mL), The four substances were dissolved in buffer solutions of three different pH(10 mM Tris-HCl system at pH 7.0, pH 8.0, and pH 9.0). The four peptides are dissolved in three buffer solutions with different pH. The pretreated clean silicon wafer was used as a substrate for the LbL assembly via coating deposition. Before assembly, the wafer was immersed in PEI (1 mg/mL) for 20 min. After a layer of PEI was coated on the substrate surface, the wafer was alternately immersed in TA and polypeptide solutions for 20 min until the required number of layers (n) was obtained. Each layer was thoroughly washed with deionized water and dried using nitrogen. The TA and peptide solutions had the same pH value during LbL assembly.

2.3. Thickness test of coating

Coating thicknesses were measured using a Woollam M2000UI (J. A. Woollam Co., Inc., Lincoln, NE) multiangle spectroscopic ellipsometer with WVASE32 analysis software for two incident angles of 65° and 70°.

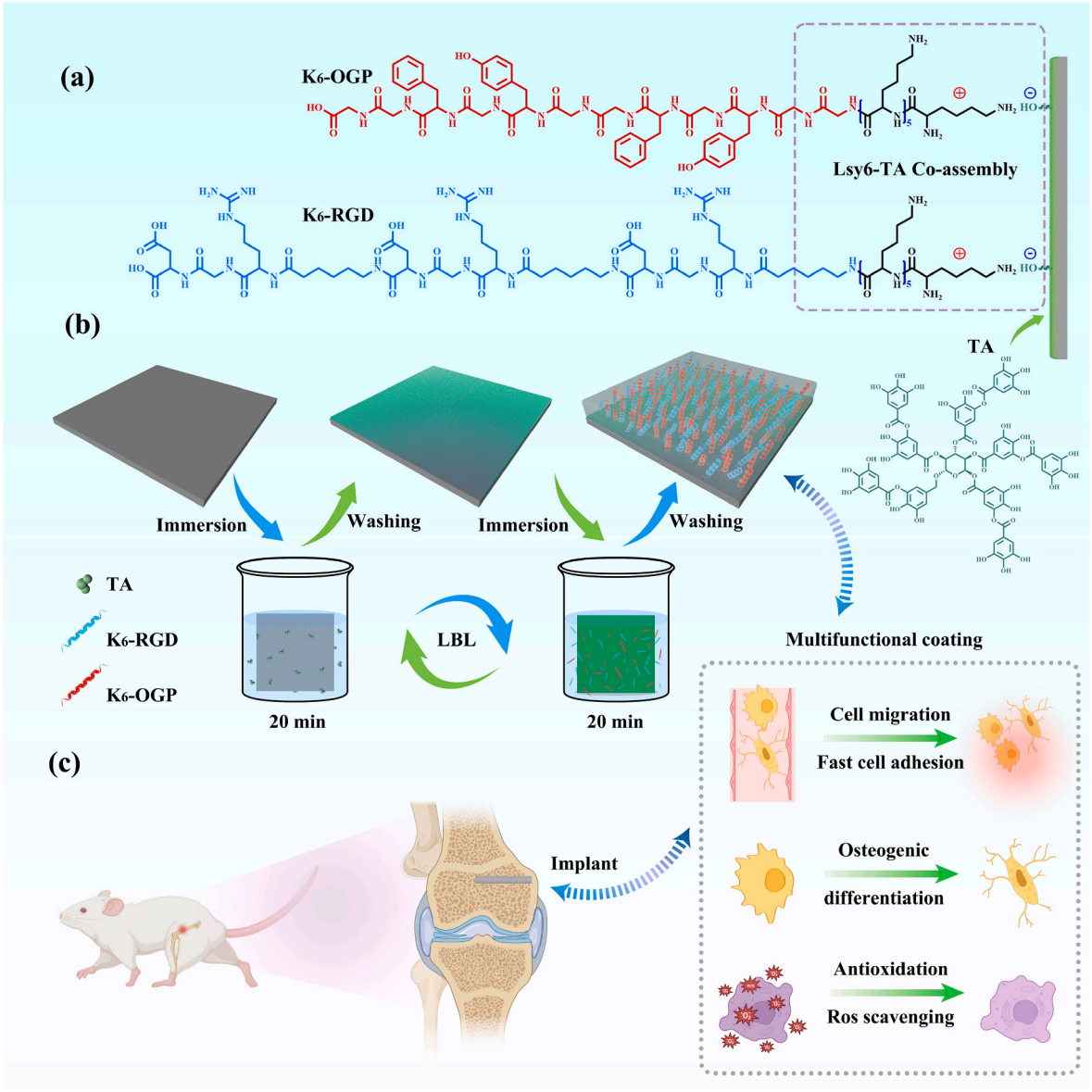

Scheme 1. (a) Schematic representation of the TA and peptide structures. (b) Schematic illustration of the experimental design and LbL assembly. (c) Biological applications of multifunctional coatings.

The Ψ (polarized angle) and Δ (phase) values were measured between 245 and 1000 nm. The Model of Spectroscopic Ellipsometry (SE) can accurately monitor the polarization angle (ψ) and phase difference (Δ) to represent the change of the polarization state of the incident light wave when it is reflected at the material interface, and calculate the quantitative information of the refractive index, thickness, and quality of the coating on the interface. These two parameters (ψ and Δ) are related to the thickness and optical properties of the sample and can be calculated by:

where rp and rs are the reflection coefficients of parallel and perpendicular directions to the plane of incidence, ρ is the complex reflectance ratio, θ_0 is the angle of incidence, h_j is the thickness of the layers, N_a, N_s, and N_j are the complex refractive indices of the ambient, substrate, and the layers, respectively.

2.4. Quartz crystal microbalance

The kinetic changes during the LbL assembly of thin films were detected using a quartz crystal microbalance (QCM-D) with dissipation. The gold-coated quartz crystal sensor was washed in a mixture of $NH_3{\cdot}H_2O$ (25 %), H_2O_2 (30 %) and H_2O (1:1:5) at 75 °C for 1 h, rinsed thoroughly with deionized water, and dried using nitrogen. The chip was installed in the flow chamber of Q-Sense and Tris-HCl buffer was passed across it until the system reached equilibrium. Thereafter, TA, buffer, peptide, and buffer was passed in sequence across the chip, each for 20 min, until the assembly reached the required number of layers (n). The flow rate of the injected solution was 50 μL/min, and the energy dissipation (ΔD) and resonance frequency (Δf) changes under different overtones ($\nu = 3, 5, 7, 9 \ldots$) were monitored in real time; data when $\nu = 3$ were used to draw the image.

2.5. Mechanical properties and surface morphology analysis of the coating

The surface mechanical properties, surface morphology, adhesion energy, and roughness of the coating were measured using an atomic

force microscope (AFM; Dimension Icon, Bruker). First, the sample was placed on the AFM sample table and fixed using vacuum adsorption; then, the surface of the coating sample was characterized in MikroMash silicon cantilever percussion mode and the roughness was calculated by a subsidiary software. To calculate the Young's modulus, the retract curve of the force versus separation plots was fitted using the Derjaguin–Muller–Toporov model.

2.6. Characterization of water contact angle of coatings

The water contact angle was measured using the static contact drop method on the KRUSSDSA1 version 1.80 droplet shape analyzer, with deionized water used as the probe titration liquid.

2.7. Coating stability test

The prepared TA-polypeptide coating was immersed in PBS buffer, and the film thickness was measured at 1, 2, 3, and 4 weeks. The experiment was carried out at normal temperature. The stability of the coating was calculated as the change of film thickness with immersion time.

2.8. Quantitative determination of polypeptides by fluorescence labeling

MCA-labeled RGD and TAMRA-labeled OGP were prepared to visualize the adsorption of the two peptides on the substrate surface. RGD: OGP were mixed in different volume ratios (5:5, 8:2, and 3:7) in the dark as required for LbL assembly. Thereafter, the polypeptide distribution and fluorescence intensity before and after assembly were monitored under confocal laser light. The standard curves of the two fluorescently labeled peptides were measured separately using a UV spectrophotometer. Finally, the absorbance of the remaining fluorescent peptides at different ratios in the solution before and after assembly was measured, and the peptides were quantified using standard curves.

2.9. Cell adhesion test

MC3T3-E1 cells (2.5×10^4) were seeded in 24-well plates, and divided into blank, positive control, $(TA\text{-}RGD)_6$, $(TA\text{-}OGP)_6$, and $(TA\text{-}OGP@RGD)_6$ groups. A glass slide coated with collagen solution acted as the positive control group. After culturing in the cell incubator for 12 h, the plates were shaken at 150 rpm for 30 min, and the cell viability of each group was detected using the CCK8 kit to indirectly illustrate the adhesion of the cells onto the coating surface.

2.10. Cell culture

MC3T3-E1 cells derived from mouse bone marrow was purchased from Punosi and cultured in α-MEM basic medium supplemented with 100 U/mL penicillin, 100 mg/mL streptomycin, and 10 % FBS at 37 °C with 5 % carbon dioxide. On the second day, cells were cultured in a 25-mm^2 flask and grown to an 80 % density.

2.11. Cell migration

MC3T3-E1 cells (2.5×10^5) were inoculated on slides in a 6-well plate. After culturing for 24h, a sterile 100-μL pipette tip was used to make three uniform vertical scratches on the slides of each well. After washing the slides with PBS, the medium was replaced with serum-free medium for 24 h. The cells that migrated to the scratched area were observed using inverted fluorescence microscope.

2.12. Early cell adhesion and spreading

MC3T3-E1 cells (4×10^4) were inoculated on blank slides in 24-well plates and the circular slides were coated with peptide materials. After 2 and 4 h of culturing, the cells were fixed with 4 % paraformaldehyde, and then 0.1 % TritonX-100 was added to disrupt the cell membrane. The cytoskeleton and nuclei were then stained with rhodamine (red) and DAPI (blue) labeled with cyclopeptide, respectively. Changes in the cell number and morphology were observed using laser confocal scanning microscope (CLSM), and the cell adhesion and spreading area were counted using ImageJ.

2.13. Cell viability and proliferation

MC3T3-E1 cells (1×10^4) were inoculated on blank and coated slides in 24-well plates. The culture medium was changed every 1–2 days, and the cell viability was detected using a CCK8 kit on days 1 and 3. Cells were fixed using paraformaldehyde on day, and the cytoskeleton and nucleus were stained with rhodamine (red) and DAPI (blue) labeled with cyclopeptide. Cell proliferation was observed using CLSM.

2.14. Antioxidant activity test

Using a FRAP kit, a standard curve was plotted to examine the relationship between concentration and strength of iron reduction and antioxidant capacity. The reaction solution (540 μL) was added to the sample of the coating material and incubated at 37 °C for 5 min. The solution was then transferred to a 96-well plate, and the absorbance of the sample was measured at 593 nm using a spectrophotometer. The antioxidant activity of different substrates was determined using the same method.

2.15. Intracellular ROS scavenging

MC3T3-E1 cells (4×10^4) were inoculated on blank and coated slides in 24-well plates. After 24 h of culturing, negative and positive controls were established, and the normal medium was replaced with H_20_2 (300 μM) stimulation medium. After stimulation for 12 h, the intracellular ROS detector DCFH-DA probe was added and incubated for 20 min. Cells were then fixed with 4 % paraformaldehyde, and the nuclei and cytoskeleton were stained. The effect of scavenging ROS was calculated based on the fluorescence intensity of ROS before and after stimulation, as well as the changes in cell morphology and number.

2.16. Osteogenic staining analysis

Early osteogenic differentiation is characterized by alkaline phosphatase (ALP) activity, and alizarin red S is an indicator of calcium deposition. MC3T3-E1 cells were inoculated at a density of 2×10^4 cells/well. At days 7 and 14, cells were fixed with 4 % paraformaldehyde. ALP activity was then detected using the BCIP/NBT kit and cells were visualized using a microscope. On days 14 and 21, cells were stained with 0.1 % alizarin red S solution for 30 min (pH 4.2). After fixing, the cells were washed with PBS three times, and 10 % cetylpyridinium chloride solution added for 1 h. The absorbance at 593 nm was measured to quantify the calcium nodules.

2.17. Osteogenic genes expression

MC3T3-E1 at 2×10^4 cells/well were seeded onto $(TA\text{-}OGP@RGD)_6$ coatings. After 14 days of culturing, the RNA of MC3T3-E1 cells was extracted using TRIzol reagent and reverse transcribed to cDNA using the PrimeScript RT kit. β-actin was used as the housekeeping gene, and the forward and reverse primers for osteogenesis-related genes are listed in Table S1. Data were analyzed using the $2^{-\triangle\triangle ct}$ method were normalized to the mean values of the control group.

2.18. In vivo osteogenesis evaluation

2.18.1. Implantation surgery

All protocols involoving animals were approved by the Wenzhou Research Institute of National Science. All procedures were performed according to the standard guidelines described in the Guide for the Care and Use of Laboratory Animals.

Nine healthy 8-weeks old male Sprague–Dawley rats (weight, 270–300 g) were housed in cages for 2 weeks, following which they were randomly assigned to three groups (three replicates per group). Before surgery, all animals were anesthetized using an intraperitoneal injection of 2 % pentobarbital sodium (Sigma Aldrich, USA) at a dose of 3 mL/kg body weight. After shaving their hind limbs, the rats were immobilized in the supine position. Thereafter longitudinal skin incisions were made, and a cylindrical hole 1.2 mm in diameter and 10 mm in length were made in the direction of the major axis of femur. The prepared titanium implant was then gently inserted in the holes. Two implants with different modified surfaces were placed in each rat with one implant per femur. After surgery, the soft tissues were closed, and the skin was sutured. After 5 and 8weeks, the rats were euthanized using sodium pentobarbital, and the bilateral femurs were removed and fixed in 4 % paraformaldehyde, respectively.

2.18.2. Microcomputed tomography analysis

Microcomputed tomography (micro-CT) was used to photograph the distal femur with the following parameters: voltage, 80 kV; current, 300 mA; and 360° rotation with a 0.5° rotation step. The focus was on new bone formation between bone tissue and implants. Briefly, the region of interest around the distal femur was reconstructed using the affiliated software (CTAn and CTVol), and the bone volume (BV) and total volume (TV) of bone were generated.

2.18.3. Biomechanical pullout test

The bone-to-implant binding strength was evaluated using the pushout test. The sample was mounted on an Instron E10000 (Instron, USA) equipped with a 500-N manometer, and the titanium rod was pulled out from the bone at a displacement rate of 1 mm/min until complete separation.The maximum failure load was recorded.

2.18.4. Histology and histomorphometry

Hard tissue sectioning was used to characterize the bone bonding effect at the bone-implant interface. Briefly, all samples were fixed with paraformaldehyde, washed by double-distilled water, dehydrated using ethanol, made transparent using xylene, and then embedded in polymethyl methacrylate. The embedded block was cut into 300-μm thick slices along the longitudinal axis and implantation center using a hard tissue slicer (EXAKT300CP), and then cut into 10-μm-thick slices using a grinding system (EXAKT400CS). The samples were stained with toluidine blue and visualized using optical microscope (OLYMPUSBX43). Bone-implant contact (BIC, the percentage of implant perimeter in direct contact with bone tissue in the implant area) was calculated using Image-Pro Plus software.

2.19. Statistical analyses

All data are reported as the average of at least three duplicates, with the error bar indicating the standard deviation. At least 10 randomly selected images were used to analyze cell numbers and cell area using Image J (https://imagej.net/downloads). Statistical analyses were performed using single-factor analysis of variance (ANOVA) and two-factor ANOVA for comparisons. The significance was noted as * $p < 0.05$, ** $p < 0.01$, *** $p < 0.001$, and **** $p < 0.0001$.

3. Results and discussion

3.1. Coating preparation and deposition process

TA is a natural polyphenol derived from plants and is rich in phenolic hydroxyl groups. It can combine with various bioactive molecules through covalent and noncovalent interactions [29]. Further, pH is an important factor regulating the growth mode of the LbL assembly. Therefore, we first explored the changes in film thickness during the self-assembly of TA with OGP and RGD under different pH conditions and investigated the optimal pH for the assembly of TA and OGP@RGD hybrid peptides. Ellipsometry is an optical method of recording the polarization change when reflected on the surface of the sample. The relative polarization changes can indicate the changes in ellipsometry parameters, refractive index n, and optical thickness, enabling the deduction of the film thickness [30,31]. Based on the ellipsometer measurements (Fig. S1), at pH 7, the film thickness of the TA–OGP (~66 nm) assembled with seven double layers was similar to that of TA–RGD (~68 nm) (Fig. S1a). At pH 8, the film thickness of $(TA\text{-}RGD)_7$ was as thick as 60 nm and the film thickness of $(TA\text{-}OGP)_7$ was >45 nm (Fig. S1b). At pH 9, the film thicknesses of both $(TA\text{-}RGD)_7$ and $(TA\text{-}OGP)_7$ could only reach approximately 35 nm (Fig. S1c). Thus, the assembly effect of TA with OGP or RGD was optimal at pH 7 and the binding ability of the two peptides of RGD or OGP to TA was the same. Therefore, the mixture of TA and OGP@RGD (1:1) at pH 7 was used to analyze the thickness of the self-assembled monolayers. The growth trend of the membrane thickness of $(TA\text{-}OGP@RGD)_7$ was similar to that of the single peptide, and the membrane thickness was ~70 nm (Fig. 1a).

QCM-D is a mass-sensitive sensor that can detect the molecular adsorption on the surface of biomaterials. It is also used to measure adsorption mass, adsorption thickness, viscoelasticity change, and adsorption conformation change [32]. To accurately determine whether the binding ability and reaction rate of the RGD and OGP peptides to TA were consistent, QCM-D was used to monitor and analyze the coating self-assembly deposition process, and the polypeptide adsorption quality at pH 7 was measured. The frequency of RGD, OGP, and OGP@RGD peptides gradually decreased in the six bilayer assemblies (Fig. 1b–d), indicating that TA and the peptides were successfully assembled on the chip surface. We also observed that the frequency shift of TA with OGP, RGD, and mixed peptides were similar, indicating that the mass deposition of TA and the three peptides is fundamentally the same. The frequency curves of the three peptides were subjected to kinetic fitting (Figs. S2d–f); the results are shown in Table S2. After ExpDec1 model fitting, the reaction slope of TA with OGP peptides was 124.30 ± 2.71 and those of RGD and OGP@RGD were 116.00 ± 1.83 and 100.94 ± 2.89, respectively. The reaction rates of the three peptides were similar to those of TA. Following this, the adsorption quality of the three peptides was analyzed. It was observed that the adsorption quality gradually increased with an increase in the number of deposition layers. After depositing six bilayers, the density of the three peptides did not significantly differ, with all reaching 3500–4000 $\mu m/cm^2$ (Fig. S2a). The function curve of the film thickness and the number of deposited layers was obtained by fitting the acoustic Voigt and Sauerbrey model (Figs. S2b and c), and this was consistent with the adsorption curve of the polypeptides. This evidence confirmed the consistency of the binding ability and reaction rate between the RGD and OGP peptides and TA. Therefore, OGP@RGD mixed peptides and TA can be assembled while retaining the structural characteristics of RGD and OGP.

3.2. Surface characterization

Surface properties such as mechanical properties, roughness, adhesion energy, stability, and hydrophilicity of the coating under physiological conditions can affect biological function [33]. First, the coating must be sufficiently stable to maintain a long-term curative effect in vivo. Fig. 1e presents the variation in the thickness of the assembled

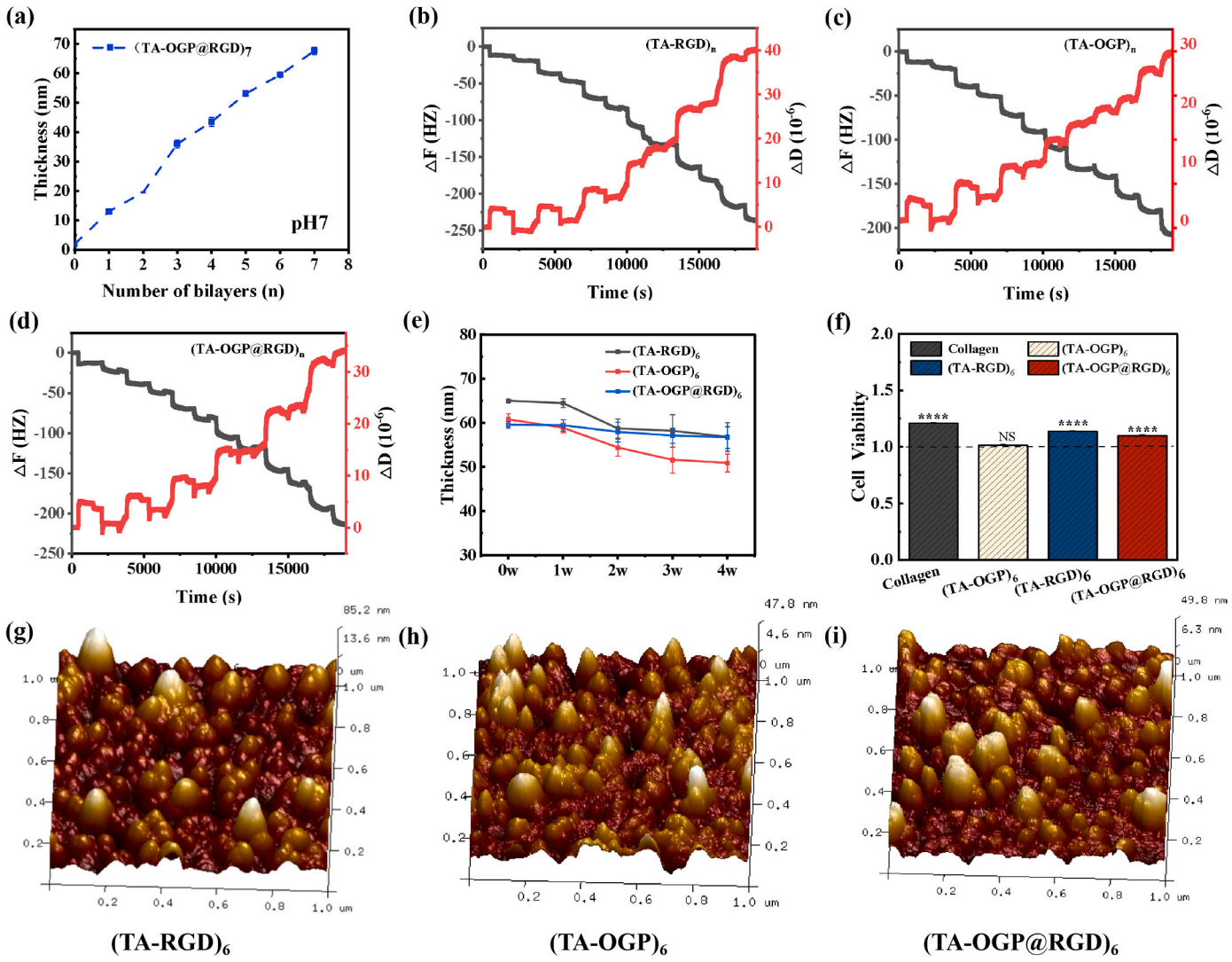

Fig. 1. (a) Analyses of the layer thickness of the mixed TA and OGP/RGD peptides (1:1) at pH 7. QCM-D analysis of six bilayers of TA and different peptides self-assembled deposition at pH 7 showing frequency and dissipation changes as functional curves of time (b) (TA-RGD)n, (c) (TA-OGP)n, and (d) (TA-OGP@RGD)n. (e) Thickness of the coating changes with time in PBS solution. (f) Cell adhesion under shear force. (g–i) AFM images of $(TA\text{-}RGD)_6$, $(TA\text{-}OGP)_6$, and $(TA\text{-}OGP@RGD)_6$ coatings in air environment.

coating immersed in PBS over time. In the first 2 weeks, the coating thickness decreased within the normal range and began to stabilize in the third week. By the fourth week, the coating thickness decreased by approximately 8 nm, indicating that the coating was sufficiently stable under physiological conditions. Thereafter, the adhesion of the different coatings was evaluated based on the viability of cells on the coated surface under centrifugal force. The results indicated that the viability of cells grown on $(TA\text{-}RGD)_6$, and $(TA\text{-}OGP@RGD)_6$ did not significantly differ from that of those grown on collagen; however, the cells grown on $(TA–OGP)_6$ performed poorly (Fig. 1f). To examine the mechanical properties of the coating surface, the structure and performance of different bioactive coatings in gas and liquid phases were tested using AFM. In the gas phase, the morphology of the three coatings modified by peptides was relatively close, with all exhibiting discontinuous rough structures (Fig. 1g–i), and Young's modulus and adhesion energy of the $(TA\text{-}RGD)_6$ coating showed the best effect, compared with the other two peptide coatings. (Fig. S3). Fig. 2a–c shows the surface morphology of the coating in liquid environment. The coating surface exhibited a discontinuous rough structure, and the roughness was fitted using the Nano Scope analysis software. The roughness of $(TA\text{-}RGD)_6$ was 17.5 nm, which was higher than that of $(TA\text{-}OGP)_6$ and $(TA\text{-}OGP@RGD)_6$. According to the JKR theoretical equation reflecting the coating adhesion, the surface adhesion of the polypeptide coating was obtained, and the adhesion energy of $(TA\text{-}RGD)_6$, $(TA\text{-}OGP)_6$, and $(TA\text{-}OGP@RGD)_6$ were 3.6, 4.4, and 3.4 μN m^{-1} (Fig. 2d–f). The adhesive ability of $(TA\text{-}OGP)_6$ was higher than that of $(TA\text{-}RGD)_6$ and $(TA\text{-}OGP@RGD)_6$ in the liquid environment, but not in the gas environment. The difference in adhesive ability may be due to differences in the hydration of the polypeptide coatings, which are influenced by the test environment (liquid or gas). Moreover, $(TA\text{-}RGD)_6$ exhibits greater hydrophilicity than $(TA\text{-}OGP)_6$, which leads to a softer and more porous coating surface when exposed to a liquid environment. As a result, the adhesion energy of RGD is reduced when compared to the gas phase. No significant difference was found in the Young's moduli of the three types of polypeptide coatings (Fig. 2g–i) of approximately 20–25 MPa. The morphology of the polypeptide coating obtained in the air environment was not significantly different from that in the liquid environment, although the Young's modulus and adhesion of the polypeptide coating obtained in the air environment are higher than those in the liquid environment.

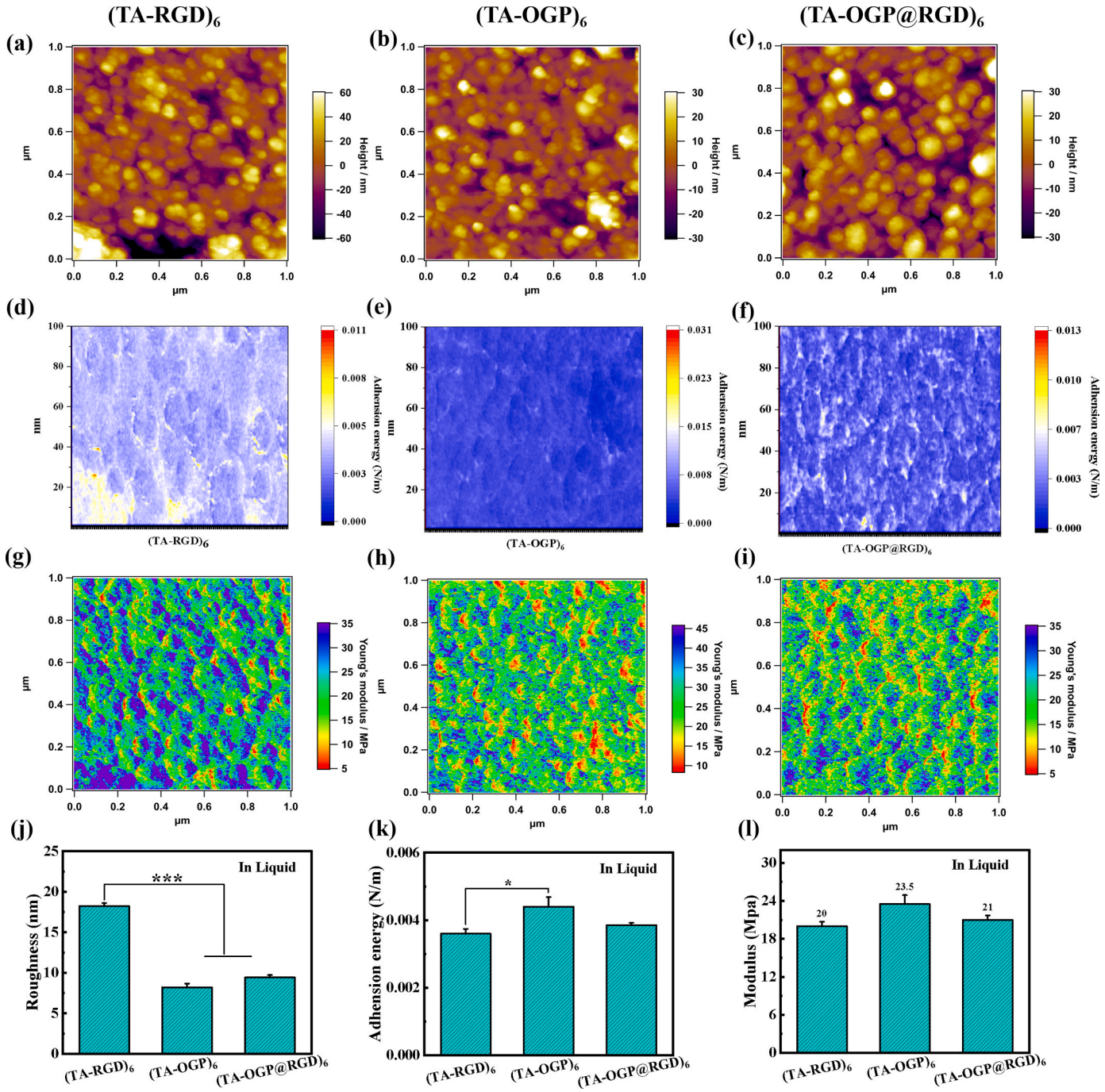

Fig. 2. (a–c) AFM images of $(TA\text{-}RGD)_6$, $(TA\text{-}OGP)_6$, and $(TA\text{-}OGP@RGD)_6$ coatings in a liquid environment. (d–f) Adhesion energy images of $(TA\text{-}RGD)_6$, $(TA\text{-}OGP)_6$, and $(TA\text{-}OGP@RGD)_6$ coatings in a liquid environment. (g–i) Young's modulus images of $(TA\text{-}RGD)_6$, $(TA\text{-}OGP)_6$, and $(TA\text{-}OGP@RGD)_6$ coatings in a liquid environment. (j) Surface roughness of $(TA\text{-}RGD)_6$, $(TA\text{-}OGP)_6$, and $(TA\text{-}OGP@RGD)_6$ coatings in a liquid environment. (k) Quantitative analysis (d–e) of adhesion energy in a liquid environment. (l) Quantitative analysis (g–i) of shear modulus in a liquid environment.

To further confirm the successful grafting of TA and the peptides, we conducted an analysis of the coating components using XPS. In Table S3, you can observe the atomic ratios of TA and the peptides. Additionally, in Figs. S4a and b, the appearance of the N peak indicates the successful binding of the two components. Further analysis of the N1s peak reveals the absence of C═N double bonds (Figs. S4c and d), allowing us to exclude the possibility of Schiffbase covalent interactions between TA and the peptides. Previous studies have indicated that hydrophilicity is not only conducive to the adsorption of proteins on the coating surface but also to early cell adhesion; moreover, it effectively promotes osseointegration [34]. The contact angle of the biomaterial surface, measured using the contact angle meter, can reveal the hydrophilicity and hydrophobicity of the sample and is widely used to prove the effectiveness of the surface modification scheme [35]. The contact angle of $(TA\text{-}OGP)_6$-modified material was 38.65° and that of $(TA\text{-}RGD)_6$--modified material was 24.42° (Figs. S5a and b) After modification with the compound polypeptide $(TA\text{-}OGP@RGD)_6$, the contact angle (31.75°) was between the two peptides. Compared with the single metal substrate, the interface modified by two types of peptides had improved hydrophilicity to promote cell adhesion and growth.

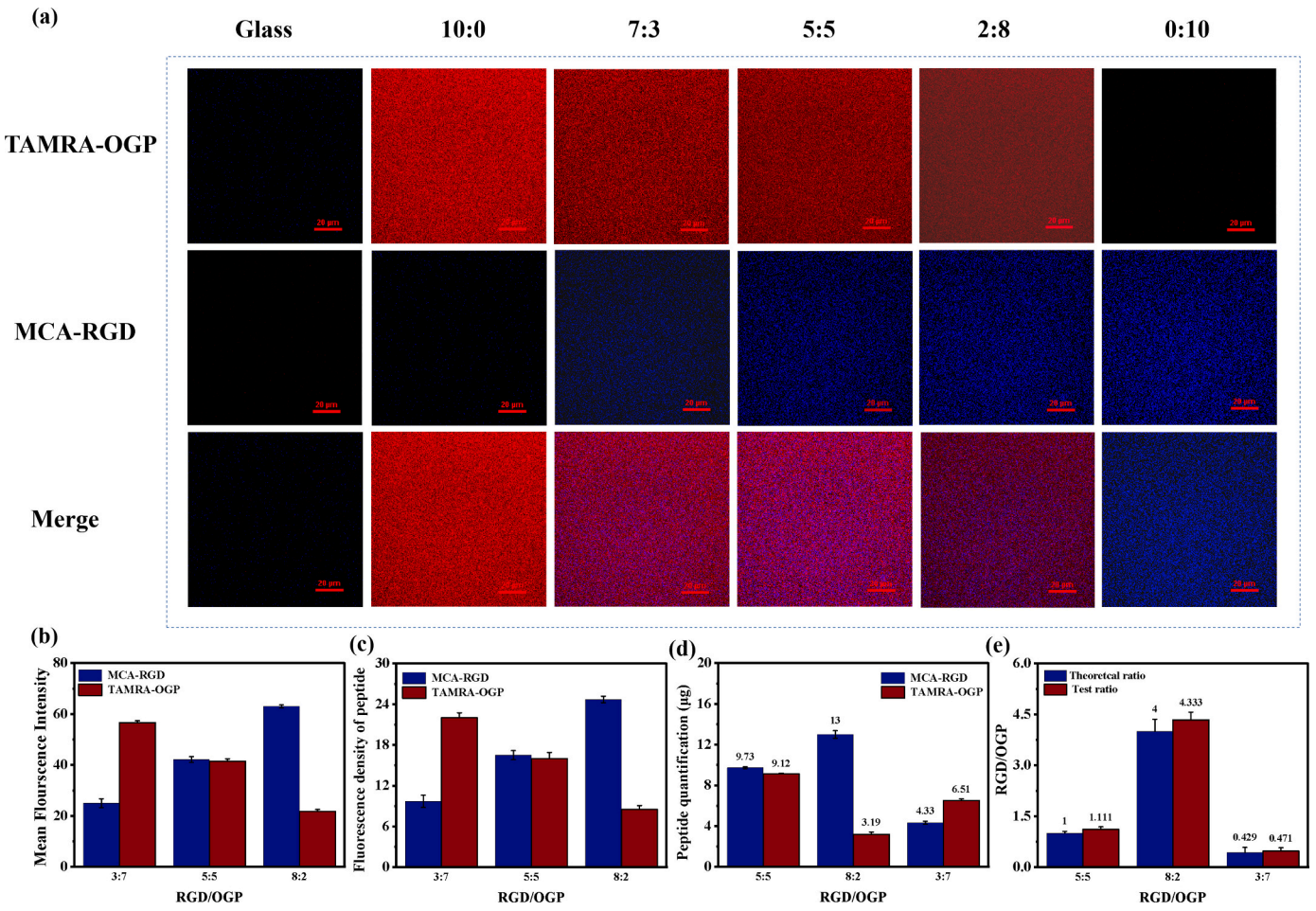

Fig. 3. Quantification of peptide content on the mixed peptide–decorated glass surfaces via fluorescent labeling. (a) Visualization of fluorescently labeled peptides (TAMRA-OGP peptide and MCA-RGD peptide) immobilized on glass substrates (Scale bar = 20 μm). (b) Average fluorescence intensity of the peptides-decorated substrates with different volume ratios (n = 6). (c) Quantitative peptide density of the peptide-decorated substrates with different volume ratios (n = 6). (d) Determination of polypeptide content with different volume ratios (n = 6). (e) Comparison of the actual and theoretical ratios of the two peptides.

3.3. Quantification of peptide content via fluorescent labeling

The above results confirmed that these peptides bind to the modified substrate surface; therefore, it was important to determine whether they were immobilized at the preset volume ratio. The fluorescence distribution of different experimental groups was uniform, indicating the uniformity of surface peptides (Fig. 3a). In addition, in the samples treated with different peptide ratios, the intensity of red light (OGP) gradually decreased and that of blue light (RGD) gradually increased, indicating that the OGP and RGD peptides were successfully adsorbed on the substrate surface at the designed ratio. The average fluorescence intensity and peptide density of different experimental groups were quantified (Fig. 3b and c), and the results confirmed that the trend of fluorescence intensity change was consistent with the peptide ratio. The amount of final peptide on the substrate surface was quantified using a standard curve (Fig. S6). Fig. 3d and e shows that at a 5:5 ratio of OGP/RGD, the amount of MCA-RGD and TAMRA-OGP was 9.73 and 9.13 μg, respectively, and the ideal and actual ratios were 1.11:1, respectively. Other ratios exhibited similar results; therefore, we considered that the two peptides were immobilized at the preset volume ratios. This result preliminarily demonstrates the possibility of the hypothesis through the joint connection of K6 peptide and LbL self-assembly to achieve the regulation of the ratio of the two peptides.

3.4. Early cell adhesion and diffusion

Cell adhesion is the first biological behavior after bone biomaterial implantation, that has an important impact on subsequent proliferation, differentiation, and osteogenesis [36]. Osteoblasts differentiate from mesoderm mesenchyma and can secrete bone matrix, the main component of which is type I collagen. After the formation of collagen fibers, the vesicular structure containing calcium, phosphorus and other components in the cytoplasm of osteoblasts will be released and deposited on the collagen fibers to form crystallized apatite to mineralize the bone matrix [37]. Therefore, the early adhesion and diffusion of osteoblasts is key to favorable osseointegration. After MC3T3-E1 cells were inoculated on the surface of the material for 2 and 4 h, the adhesion of cells in the early stage on the coatings of $(TA\text{-}OGP)_6$, $(TA\text{-}RGD)_6$, and the mixed peptides at different ratios were observed vis fluorescence microscopy, and a glass slide was used as a control. At 2 h after inoculation, the cells on $(TA\text{-}OGP)_6$ were slightly diffused compared with those on the glass surface (Fig. 4a). Cells on $(TA\text{-}RGD)_6$ and hybrid peptide-modified surfaces exhibited significant spreading. Cells in all samples spread further at 4 h compared with those at 2 h. The cell shape was clear at 4 h especially for the mixed polypeptides at different ratios and was relatively close to the fully expanded shape of osteoblasts. To evaluate the cell adhesion and diffusion, two important indexes, cell number and cell area, were used. The area and number of cells per mm^2 are shown in Fig. 4b and c. At 2 and 4 h, the number of cells adhered to

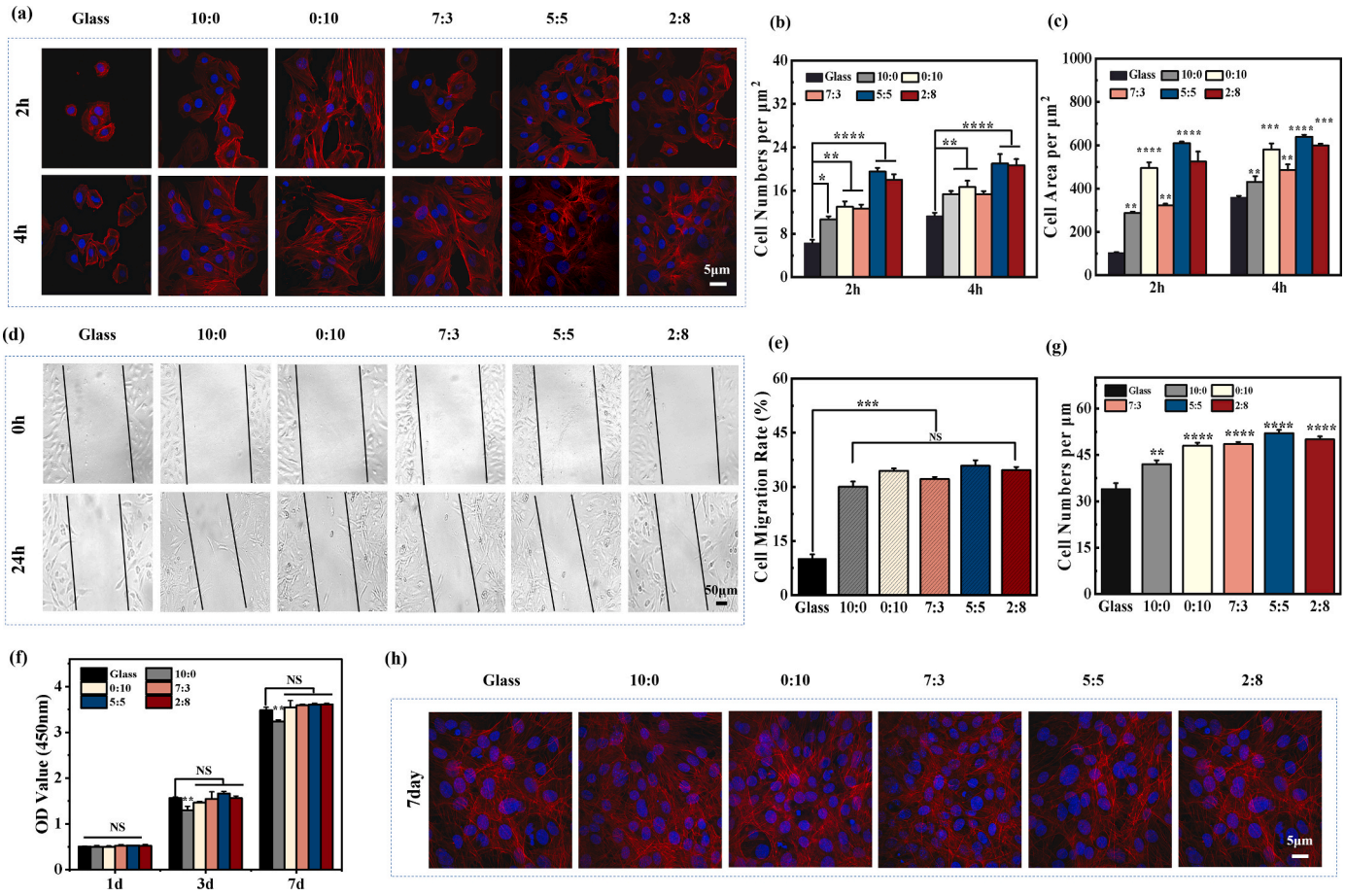

Fig. 4. (a) Fluorescence microscope images of MC3T3-E1 cells seeded on different coatings for 2 and 4 h; (b) Number of MC3T3-E1 cells per μm^2 on different coatings; (c) Cell area of MC3T3-E1 cells per μm^2 on different coatings (d) Cell migration on glass, $(TA\text{-}OGP)_6$, $(TA\text{-}RGD)_6$, and mixed peptides in different proportions for 0 and 24 h, respectively. (e) Quantitative analysis of cell mobility in (a). (f) Histogram of cell viability with glass, $(TA\text{-}OGP)_6$, $(TA\text{-}RGD)_6$, and mixed peptides in different proportions in cultures at day 1, 3, and 7. (g) The number of nuclei of cells cultured on coating for 7 days (difference analysis and results are compared with glass in the same period). (h) Fluorescence microscope images of MC3T3-E1 cells cultured on different coating surfaces for 7 days.

the $(TA\text{-}OGP)_6$ film was slightly higher than that of the control, consistent with the fluorescence images. The number of $(TA\text{-}RGD)_6$ cells was 3-fold higher than that of the control group at 2 h and then decreased to 1.5-fold at 4 h. When OGP and RGD were assembled at a 5:5 ratio, the number of cells was 4-fold that of the control group at 2 h and significantly different at 4 h. For the cell area (Fig. 4c), the cell area on the $(TA\text{-}OGP)_6$ membrane was slightly higher than that on glass at 2 and 4 h, and $(TA\text{-}RGD)_6$ and mixed peptides at the 5:5 ratio were significantly different from those on glass at 2 and 4 h. This could explain why cells on the $(TA\text{-}RGD)_6$ and mixed peptide 5:5 ratio membranes spread faster than cells on glass. In both time periods, cell area and number were the highest at the 5:5 ratio.

3.5. Cell migration

The migration of osteoblasts is an important physiological event involved in bone healing and remodeling. Osteoblasts migrate to the bone defect site, which supports their proliferation and differentiation [38]. After 24 h, the cells migrated to varying degrees on the surface of each material (Fig. 4d). For the migration area of cells on the coating surface, the migration effect of mixed peptides in different proportions was optimal at 43 % (Fig. 4e). The migration area did not differ between treatments with OGP or RGD alone but significantly differed from the control group. $(TA\text{-}RGD)_6$ can effectively regulate cell behavior and induce cell migration because of the close and extensive communication between RGD peptides and cell membrane surface. The migration ability of $(TA\text{-}OGP)_6$ was similar to that of $(TA\text{-}RGD)_6$. The OGP peptide may stimulate the activity of osteoblasts and promote their growth to enable migration in osteoblast culture. However, the mixed peptides in different ratios have the advantages of both peptides, both of which promote cell migration.

3.6. Cell viability and proliferation

MC3T3-E1 cells are subcloned cells isolated from mouse embryonic osteoblast precursors and can promote osteogenic differentiation and bone matrix mineralization during osseointegration [39]. MC3T3-E1 cells were inoculated on the surface of the peptides film to evaluate the biocompatibility of TA-peptides. To quantify the proliferation of cells in the different groups, cell viability was assessed using CCK-8 on days 1, 3, and 7 of cell culturing. On these days, the cell viability was maintained at about 1.0 for the $(TA\text{-}RGD)_6$ and at different proportions of mixed polypeptide membranes (Fig. 4f), although this was not significantly different from the control. However, the viability of the cells grown on $(TA\text{-}OGP)_6$ membrane decreased slightly on days 1 and 7 and was lowest on day 3 at approximately 0.7. Thus, considering the negative electricity of the $(TA\text{-}OGP)_6$ membrane, long-term culturing is not conducive to cell proliferation (Fig. S5c). However, the membrane of $(TA\text{-}RGD)_6$ and mixed peptides neutralized the negative charge carried by TA itself and was biocompatible in vitro. To visualize the results of

CCK-8 analysis, the cytoskeleton and nucleus were fluorescently stained on day 7. The cells cultured on the coating showed good tensile morphology with no significant difference among the groups (Fig. 4g and h).

3.7. Oxidation resistance of the coating

In normal cells and tissues, ROS is in a state of dynamic equilibrium through biological elimination and production. In the nonphysiological state, such as after trauma and inflammation, the oxidative stress microenvironment is unbalanced, releasing a large amount of ROS, destroying the cell membrane and corresponding lipids, and causing failed osseointegration. Therefore, it is crucial for the implant surface coating to have ROS-scavenging ability. MC3T3-E1 cells were treated with H_2O_2 to simulate the release of ROS in vivo and the cytoskeleton and nuclei were stained (Fig. 5a). In the fluorescence images, the nuclei of the glass group stimulated by H_2O_2 had shrunk and the cell morphology was narrow and lengthened. However, the cells on the membrane with different proportions of mixed peptides were not significantly affected. The number and area of cells in the control group decreased compared with those before H_2O_2 treatment, whereas the number and size of cells on the coating did not significantly change in the other five analyzed groups (Fig. 5b and c). The number and area of cells on the membrane coated with RGD alone and with the 5:5 ratio of OGP/RGD were the highest of the groups, with no significant difference before and after stimulation. An ROS probe was added to the cells to determine the intracellular ROS content according to the immunofluorescence intensity. The green fluorescence intensity of the four groups stimulated by H_2O_2 was significantly higher than that of the unstimulated group, indicating that the H_2O_2 model was successful in inducing ROS (Fig. 5d). Before and after H_2O_2 stimulation, the fluorescence intensity of the other five groups of coatings decreased in varying degrees compared with that of the glass surface. The average fluorescence intensity on the glass surface reached approximately 90 % before H_2O_2 stimulation and decreased to approximately 60 % on the rest of the polypeptide coatings (Fig. 5e and f). After H_2O_2 stimulation, the average fluorescence intensity on the glass surface was approximately 60 % but decreased to about 30 % on the rest of the polypeptide coatings. Therefore, we considered that the coating surface has an excellent ROS-scavenging ability.

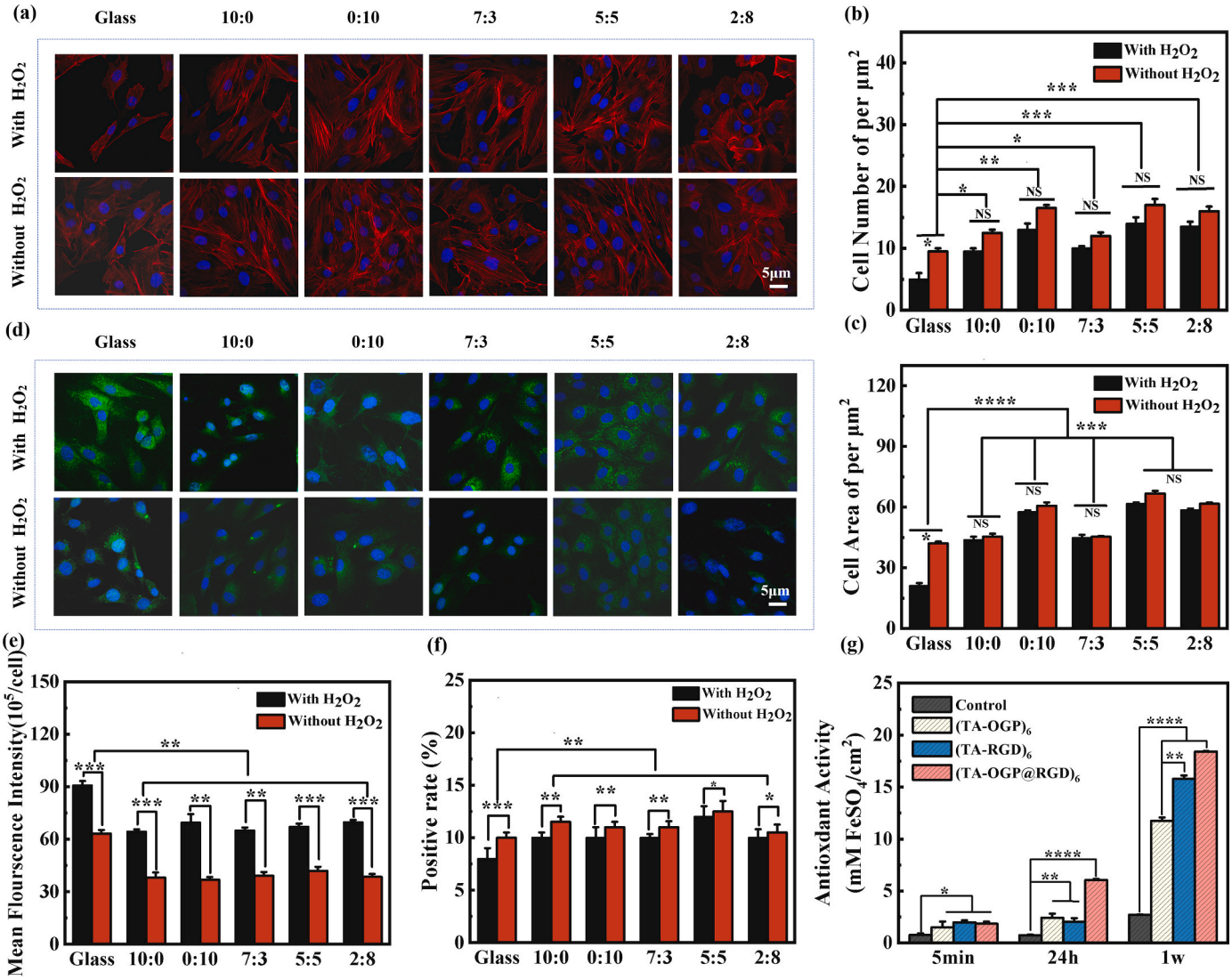

Fig. 5. Oxidation resistance of the coating: (a) Fluorescence microscope images of MC3T3-E1 cells on different coating surfaces before and after treatment with 300-μM H_2O_2. (b) The number of cells per μm^2. (c) Cell area on the coating before and after H_2O_2 stimulation. (d) Fluorescence microscope images of ROS levels in MC3T3-E1 cells on different coating surfaces before and after H_2O_2 stimulation. (e) Average fluorescence intensity of intracellular ROS before and after H_2O_2 stimulation. (f) Positive rate of intracellular ROS levels generated by cell counting. (g) Oxidation resistance of the coating was measured using a FRAP kit at 5 min, 24 h, and 1 week.

Antioxidant properties are crucial to the success of the implant; therefore, the total antioxidant capacity of the coating surface was tested using the FRAP kit. The antioxidant capacity did not differ significantly among the groups in the first 5 min. After 24 h, all coatings except the control had excellent oxidation resistance. Within 1 week, the oxidation resistance of each coating remained high. (Fig. 5g). However, the antioxidant capacity of $(TA\text{-}OGP@RGD)_6$ was higher than that of $(TA\text{-}RGD)_6$ and $(TA\text{-}OGP)_6$ tested by FRAP kit. It is influenced by multiple factors, including surface roughness, binding surface area, binding density, surface porosity, and the synergistic effect of the dual peptides, among others. These factors contribute to $(TA\text{-}OGP@RGD)_6$ having the optimal antioxidant effect, with TA being the primary component responsible for its antioxidant properties.

3.8. Analysis of osteogenic staining in vitro

ALP is an extracellular enzyme produced by osteoblasts, and the expression and activity are clear features of osteogenic differentiation and an important index to reflect the early differentiation of osteoblasts [40,41] ALP staining was performed on the day 7 and 14 of cell culture (Fig. 6a and b). ALP activity was generally low at day 7, and a large number of unstained osteoblasts could be seen especially in the control group, only a small amount of light blue could be seen (Under the alkaline condition of pH9.2~9.8, intracellular alkaline phosphatase can hydrolyze AB-BI phosphate and release phosphonaphthol, which does not couple diazonium salt to form colored products, and the active site of alkaline phosphatase is blue), with the ALP activity being the lowest. Compared with that in the control group, the different ratios of $(TA\text{-}RGD)_6$, $(TA\text{-}OGP)_6$, and OGP/RGD showed more coloration and increased color depth. The staining range and intensity of the coating containing OGP peptides were more significant than that of the RGD coating alone. Under different ratios of OGP and RGD, the ALP activity was slightly lower at 2:8, and the best with the 5:5 mixed peptide ratio among the four groups. By day 14, the activity of ALP increased in all groups. Consistent with this trend on day 7, the ALP activity of the $(TA\text{-}RGD)_6$ group was still slightly higher than that of the control group, whereas the membrane of $(TA\text{-}OGP)_6$ and OGP/RGD (5:5) showed dense blue-purple coloration and had strong ALP activity. Thus, the $(TA\text{-}OGP)_6$ and the different ratios of OGP/RGD had an excellent ability to promote osteogenic differentiation.

Alizarin red S reacts with calcium nodules, and the effect of osteogenesis-related ECM mineralization can be confirmed by alizarin red S staining after induction and culturing in vitro [42] to reflect the induction of osteogenesis. ECM mineralization occurs late, so alizarin red S staining was performed on day 14 and 21 of cell culture (Fig. 6c and d). On day 14, little difference was observed between the experimental and control groups, and no obvious calcium nodules were observed in the experimental group. On day 21, calcium nodules were still not observed in the control group, but the staining was significantly deeper than that on day 14. The surface of $(TA\text{-}RGD)_6$ film was dyed

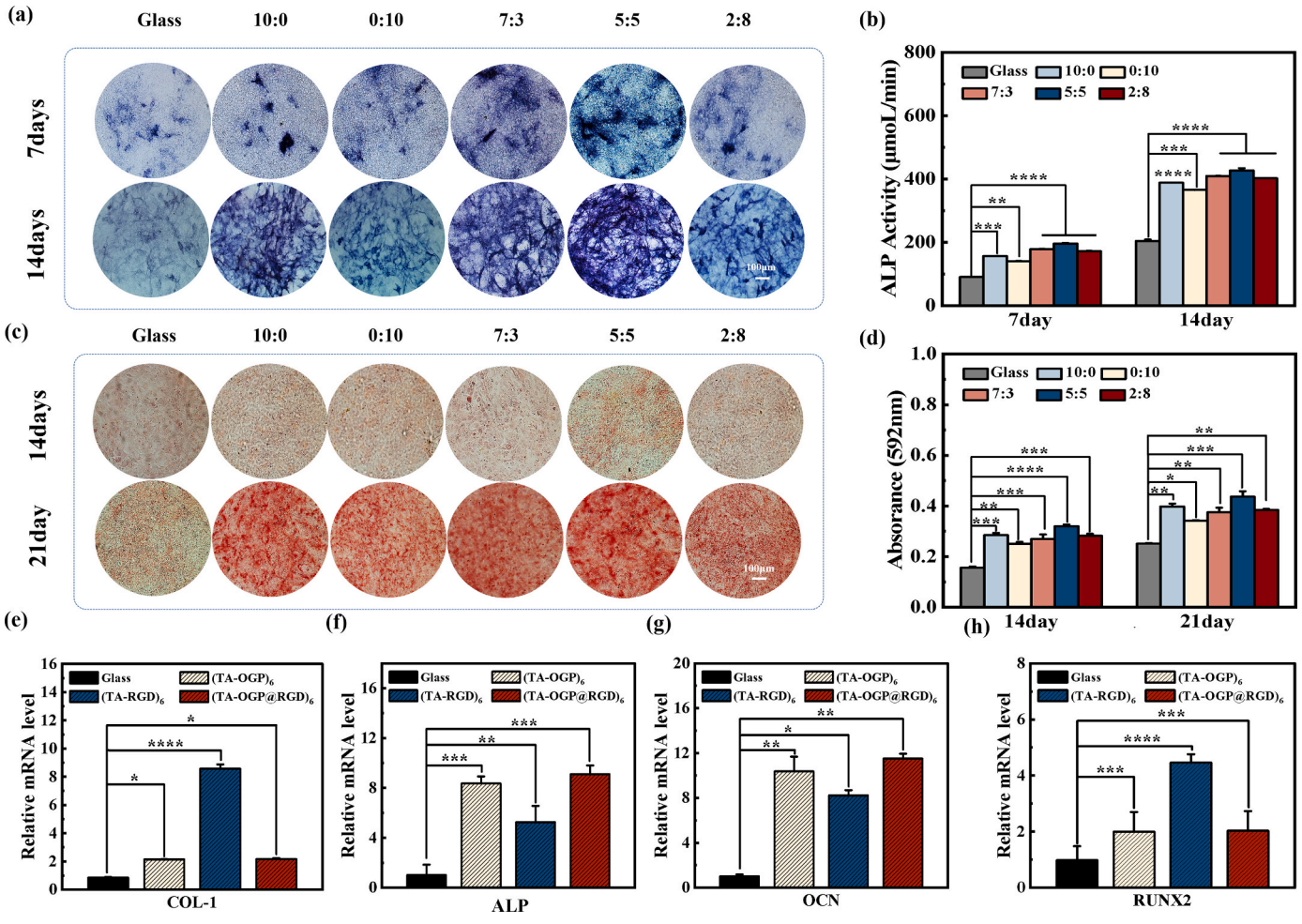

Fig. 6. Osteogenic staining analysis: (a) MC3T3-E1 cells were seeded on glass and coatings of $(TA\text{-}OGP)_6$, $(TA\text{-}RGD)_6$, and mixed peptide in different proportions and stained for ALP on days 7 and 14. (b) ALP activity quantification assay. (c) MC3T3-E1 cells were cultured on different coatings for 14 and 21 days, and alizarin red S staining was used as an indicator of bone mineralization. (d) Quantification of alizarin red S staining (n = 3); mRNA expression levels of differentiation-related proteins (e) COL-1, (f) ALP, (g) OCN, and (h) RUNX2 after culturing MC3T3-E1 cells on glass, $(TA\text{-}OGP)_6$, $(TA\text{-}RGD)_6$, and $(TA\text{-}OGP@RGD)_6$ coatings at 14 days.

reddish, and a few calcium nodules had appeared. $(TA\text{-}OGP)_6$ and different proportions of OGP/RGD did not significantly differ, the whole membrane surface was dyed red, and more dark red calcium nodules could be observed. Similar to the trend of ALP results, the 5:5 mixed peptide ratio produced the best results. Thus, $(TA\text{-}RGD)_6$ could slightly promote matrix mineralization while the single OGP coating and different proportions of mixed peptides could significantly induce ECM mineralization. The ALP activity and ECM mineralization ability of $(TA\text{-}RGD)_6$ had slightly increased compared with those of the control group. The $(TA\text{-}RGD)_6$ exhibited excellent migration and adhesion properties in the early stage, which provided a relatively favorable environment for osseointegration. OGP peptides can regulate osteogenic differentiation and induce the appearance of calcium nodules. Therefore, these peptides can induce ALP activity and promote ECM mineralization on the mixed polypeptide membrane to promote osseointegration.

Based on the above experimental studies, the synergistic effect of OGP/RGD at the 5:5 ratio was most effective and exhibited a superior ability to promote early cell adhesion, cell migration, and osteogenic differentiation. Therefore, we chose the proportion of mixed peptides at a 5:5 ratio for subsequent experiments.

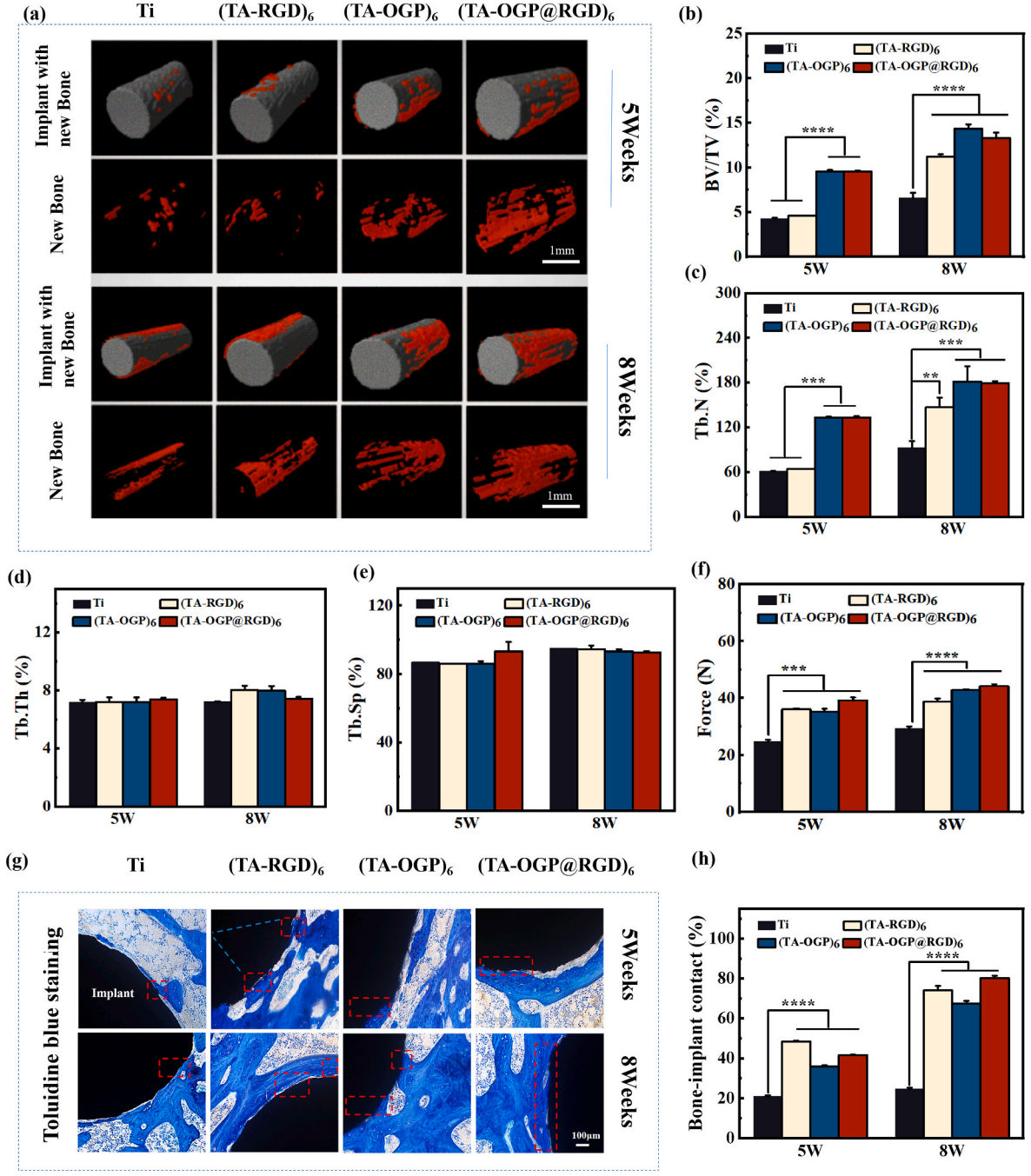

Fig. 7. Micro-CT analysis of different titanium (Ti) implants with in vivo new bone formation. (a) Representative 3D reconstruction images (red color: regenerated bone tissues). (b–e) Quantitative results of BV/TV(Bone volume fraction), Tb. N(Trabecular number), Tb. Th (Trabecular Thickness) , and Tb.Sp(Trabecular separation). (f) Average pullout strength of different peptide treated and untreated Ti screws (n = 5), the red wire frame shows the osseous integration. (g) Representative histological images of Ti-based stained with toluidine blue (Scale bar = 100 μm). (h) Average histomorphometric values of bone-implant contact (BIC).

3.9. Expression of osteogenesis-related genes

To understand osseointegration on the coating, the expression of osteogenic markers at different stages of differentiation was analyzed using RT-qPCR. COL-1 is an ECM protein that can stimulate osteoblast adhesion and differentiation [43]. ALP is a typical protein product of osteoblast differentiation, and the activity of ALP often represents the early phenotypic marker of osteoblast formation [44]; OCN appears at the end of osteogenic differentiation and binds to Ca^{2+} to regulate bone mineralization to maintain or regenerate bone tissue [45]. Runx2 is the central control protein of the osteoblast phenotype and controls the deposition of extracellular factors of COL-I and can effectively regulate the differentiation of osteoblasts [46,47].

After the cells were cultured on the coatings for 14 days, the expression of mRNA of the osteoblast differentiation markers: COL-1, ALP, OCN, and Runx2 were analyzed via RT-qPCR (Fig. 6e–h). $(TA\text{-}OGP)_6$, $(TA\text{-}RGD)_6$, and $(TA\text{-}OGP@RGD)_6$ all upregulated the expression of mRNA of osteogenesis-related proteins. Among them, the expression of COL-1 and Runx2 mRNA was the highest on the $(TA\text{-}RGD)_6$ membrane because the RGD peptide can bind to the integrin on the cell membrane. The expression of ALP and OCN mRNA in $(TA\text{-}OGP)_6$ and $(TA\text{-}OGP@RGD)_6$ was significantly upregulated, and expression with $(TA\text{-}OGP@RGD)_6$ was slightly higher than that with $(TA\text{-}OGP)_6$. Thus, $(TA\text{-}OGP@RGD)_6$ coating can induce an excellent osteogenic effect in the early and middle stage of osteogenesis, which provides an important guarantee that osteogenesis and osseointegration will occur.

3.10. Implantation experiment of coating in vivo

At 5 and 8 weeks after implantation, the titanium rods were excised along with the femoral condyle, and micro-CT scanning, pullout test, and histological staining were performed to evaluate the osteogenesis and osseointegration. CTVol software reconstructed the 3D model of femoral regeneration, as shown in Fig. 7a, where red represents the new bone. Quantitative analysis of BV fraction (TV) showed that $(TA\text{-}OGP)_6$ and $(TA\text{-}OGP@RGD)_6$ coatings produced substantial regenerated bone at 5 weeks, whereas $(TA\text{-}RGD)_6$ did not produce a significantly different effect from that in the control (Fig. 7b). At 8 weeks, $(TA\text{-}RGD)_6$, $(TA\text{-}OGP)_6$, and $(TA\text{-}OGP@RGD)_6$ coatings all contained obvious new bone. The BV/TV of $(TA\text{-}OGP)_6$ and $(TA\text{-}OGP@RGD)_6$ was 14%–15 %, and more new bone tissue was present other than that with the $(TA\text{-}RGD)_6$ coating. All three coatings contained more new bone formation than the control group, and the number of trabeculae presented the same trend (Fig. 7c).The biomechanical pullout test confirmed the enhancement of osseointegration (Fig. 7f). At 5 and 8 weeks, the connection between the titanium rod with polypeptide (single or composite) and the surrounding bone tissue was stable, which was in significantly contrast from that with bare titanium. The percentage of BIC analyzed using toluidine blue staining is the most direct evidence for evaluating osseointegration. As shown in Fig. 7g, compared with that with bare titanium, the polypeptide-coated titanium rods showed favorable osteogenesis (blue staining) at 5 weeks after implantation. At 8 weeks after implantation, although bone mineral deposition occurred on the surface of bare titanium, the bone mineral deposition was dispersed and not dense, and the interface modified by monopeptides and dipeptides had a mature bone structure. BIC is the most intuitive attribute for evaluating osseointegration. Quantitative analysis results (Fig. 7h) indicated that the BIC of bifunctional titanium rods (41.44 % ± 0.22 %) was nearly 2-fold that of bare titanium screws (20.43 % ± 0.59 %) at 5 weeks after implantation. The BIC of single OGP titanium rod (35.55 % ± 0.53 %) was significantly different from that of the control but slightly poorer than that of bifunctional titanium rod. Interestingly, a single RGD (48.72 % ± 0.47 %) presented the best osseointegration in the early stage, whereas the corresponding BV/TV did not exhibit osteogenic ability; this may be because RGD is related to the specific recognition of integrins on the cell membrane and has a considerable advantage during osseointegration. After 8 weeks of implantation, osseointegration of the single RGD titanium rod (74.04 % ± 2.22 %) was maintained along with the early Advantage, and the bifunctional titanium rods (80.24 % ± 2.06 %) exhibited the best osseointegration in the late stage. The bone integration effect of a single OGP titanium rod was slightly poorer than that of the other two groups; however, OGP plays a significant role in the maturity of new bone and the continuity of new bone formation in the late stage of osteogenesis, as can be seen in Fig. 6g. The above results prove the feasibility of our strategy, i.e., the two functional peptides can provide the required properties to the surface of TiO_2 in a simple manner, indicating that they have considerable potential in improving osseointegration in vivo.

4. Conclusion

In this study, we developed a new type of multifunctional implant coating, (TA-OGP@RGD)n, where cationic amino acids combined with RGD and OGP peptides were adsorbed layer by layer with TA under electrostatic interaction to form a composite film with multifunctional properties. The adsorption thickness of mixed peptides of TA and OGP@RGD increased linearly, and the binding constants of RGD and OGP peptides were consistent with those TA and, therefore, avoided competing with the TA reaction. AFM analysis revealed that the coating in the liquid phase maintained adhesion energy and mechanical properties. Contact angle analysis indicated that the interface modified by the coating was sufficiently hydrophilic to support cell adhesion and proliferation. Results of cell experiments indicated that this multifunctional coating improved the early migration, adhesion, osteogenic differentiation, and mineralization of osteoblasts. (TA–OGP@RGD)n exhibited favorable antioxidant properties and could maintain the intracellular ROS homeostasis. RT-qPCR analysis revealed that the expression of osteogenesis-related factors was significantly upregulated by the mixed peptides. In vivo studies demonstrated the favorable osteogenic effect of bifunctional polypeptide implants, and a large amount of new bone was formed in the early stage. Moreover, in the early and late stages of osseointegration, the BIC of dipeptide-coated titanium rods was approximately 2- and 4-fold that of bare titanium, respectively. (TA–OGP@RGD)n combines multiple functions, such as promoting early migration, adhesion, antioxidation, osteogenesis, and osseointegration, and exhibits excellent potential for the complex process of osseointegration. This may provide a new direction for the advancement of multifunctional coatings of implants.

Author contributions

B. Zhao and Y. Dong: Methodology, Formal analysis, and Writing – Original Draft, X. Shen: Methodology, Formal analysis, W. He: Date analysis, Data curation, H. Jin and L. Yao: Writing – Review & Editing, S. Zheng: Methodology , software, J. Liu and X. Zan: Funding acquisition, Supervision.

Declaration of competing interest

The authors declare that they have no known competing financial interests or personal relationships that could have appeared to influence the work reported in this paper.

Data availability

Data will be made available on request.

Acknowledgment

This work was supported by Wenzhou Key Laboratory of Perioperative Medicine (2021HZSY0069), Wenzhou Science and Technology Bureau Industrial Science and Technology Project (ZG2021033) and

Start-up Funding from Wenzhou Institute, University of Chinese Academy of Science (WIUCASQD2019009).

Appendix A. Supplementary data

Supplementary data to this article can be found online at https://doi.org/10.1016/j.mtbio.2023.100848.

References

[1] V. Goriainov, R. Cook, J. Latham, D. Dunlop, R.O. Oreffo, Bone and metal: an orthopaedic perspective on osseointegration of metals, Acta Biomater. 10 (2014) 4043–4057, https://doi.org/10.1016/j.actbio.2014.06.004.

[2] P. Brun, M. Scorzeto, S. Vassanelli, I. Castagliuolo, G. Palu, F. Ghezzo, G. M. Messina, G. Iucci, V. Battaglia, S. Sivolella, A. Bagno, G. Polzonetti, G. Marletta, M. Dettin, Mechanisms underlying the attachment and spreading of human osteoblasts: from transient interactions to focal adhesions on vitronectin-grafted bioactive surfaces, Acta Biomater. 9 (2013) 6105–6115, https://doi.org/10.1016/j.actbio.2012.12.018.

[3] M. Ramazanoglu, Y. Oshida, Osseointegration and bioscience of implant surfaces-current concepts at bone-implant interface, Implant Dentistry-A Rapidly Evolving Practice (2011), https://doi.org/10.5772/16936, 978-953.

[4] A. Zamuner, P. Brun, M. Scorzeto, G. Sica, I. Castagliuolo, M. Dettin, Smart biomaterials: surfaces functionalized with proteolytically stable osteoblast-adhesive peptides, Bioact. Mater. 2 (2017) 121–130, https://doi.org/10.1016/j.bioactmat.2017.05.004.

[5] J. Palmer, S. Flint, J. Brooks, Bacterial cell attachment, the beginning of a biofilm, J. Ind. Microbiol. Biotechnol. 34 (2007) 577–588, https://doi.org/10.1007/s10295-007-0234-4.

[6] Z. Su, J. Zhang, P. Tan, S. Zhu, N. Jiang, Selective polyetheretherketone implants combined with graphene cause definitive cell adhesion and osteogenic differentiation, Int. J. Nanomed. 17 (2022) 5327–5338, https://doi.org/10.2147/IJN.S380345.

[7] P. Zhou, X. Hou, Y. Chao, W. Yang, W. Zhang, Z. Mu, J. Lai, F. Lv, K. Yang, Y. Liu, J. Li, J. Ma, J. Luo, S. Guo, Synergetic interaction between neighboring platinum and ruthenium monomers boosts CO oxidation, Chem. Sci. 10 (2019) 5898–5905, https://doi.org/10.1039/c9sc00658c.

[8] X. Zhang, Z. Li, P. Yang, G. Duan, X. Liu, Z. Gu, Y. Li, Polyphenol scaffolds in tissue engineering, Mater. Horiz. 8 (2021) 145–167, https://doi.org/10.1039/D0MH01317J.

[9] H.Y. Tan, N. Wang, S. Li, M. Hong, X. Wang, Y. Feng, The reactive oxygen species in macrophage polarization: reflecting its dual role in progression and treatment of human diseases, Oxid. Med. Cell. Longev. 16 (2016), 2795090, https://doi.org/10.1155/2016/2795090.

[10] H. Tao, G. Ge, X. Liang, W. Zhang, H. Sun, M. Li, D. Geng, ROS signaling cascades: dual regulations for osteoclast and osteoblast, Acta Biochim. Biophys. Sin. 52 (2020) 1055–1062, https://doi.org/10.1093/abbs/gmaa098.

[11] X. Niu, Y. Fan, X. Liu, X. Li, P. Li, J. Wang, Z. Sha, Q. Feng, Repair of bone defect in femoral condyle using microencapsulated chitosan, nanohydroxyapatite/collagen and poly(L-lactide)-based microsphere-scaffold delivery system, Artif. Organs 35 (2011) E119–E128, https://doi.org/10.1111/j.1525-1594.2011.01274.x.

[12] J.W. Park, K. Kurashima, Y. Tustusmi, C.H. An, J.Y. Suh, H. Doi, N. Nomura, K. Noda, T. Hanawa, Bone healing of commercial oral implants with RGD immobilization through electrodeposited poly(ethylene glycol) in rabbit cancellous bone, Acta Biomater. 7 (2011) 3222–3229, https://doi.org/10.1016/j.actbio.2011.04.015.

[13] Y.J. Lee, J.H. Lee, H.J. Cho, H.K. Kim, T.R. Yoon, H. Shin, Electrospun fibers immobilized with bone forming peptide-1 derived from BMP7 for guided bone regeneration, Biomaterials 34 (2013) 5059–5069, https://doi.org/10.1016/j.biomaterials.2013.03.051.

[14] K. Aoki, N. Alles, N. Soysa, K. Ohya, Peptide-based delivery to bone, Adv. Drug Deliv. Rev. 64 (2012) 1220–1238, https://doi.org/10.1016/j.addr.2012.05.017.

[15] L. Padiolleau, C. Chanseau, S. Durrieu, C. Ayela, G. Laroche, M.C. Durrieu, Directing hMSCs fate through geometrical cues and mimetics peptides, J. Biomed. Mater. Res. 108 (2020) 201–211, https://doi.org/10.1002/jbm.a.36804.

[16] M. Yakufu, Z. Wang, Y. Wang, Z. Jiao, M. Guo, J. Liu, P. Zhang, Covalently functionalized poly(etheretherketone) implants with osteogenic growth peptide (OGP) to improve osteogenesis activity, RSC Adv. 10 (2020) 9777–9785, https://doi.org/10.1039/d0ra00103a.

[17] Y.C. Chen, I. Bab, N. Mansur, M. Namdar-Attar, H. Gavish, M. Vidson, A. Muhlrad, A. Shteyer, M. Chorev, Structure–bioactivity of C-terminal pentapeptide of osteogenic growth peptide [OGP (10–14)], J. Pept. Res. 56 (2000) 147–156, https://doi.org/10.1034/j.1399-3011.2000.00763.x.

[18] Y. Yang, Z. Luo, Y. Zhao, Osteostimulation scaffolds of stem cells: BMP-7-derived peptide-decorated alginate porous scaffolds promote the aggregation and osteo-differentiation of human mesenchymal stem cells, Biopolymers 109 (2018), e23223, https://doi.org/10.1002/bip.23223.

[19] C. Mas-Moruno, R. Fraioli, F. Albericio, J.M. Manero, F.J. Gil, Novel peptide-based platform for the dual presentation of biologically active peptide motifs on biomaterials, ACS Appl. Mater. Interfaces 6 (2014) 6525–6536, 10.1021/am5001213.

[20] M. Hoyos-Nogues, F. Velasco, M.P. Ginebra, J.M. Manero, F.J. Gil, C. Mas-Moruno, Regenerating bone via multifunctional coatings: the blending of cell integration and bacterial inhibition properties on the surface of biomaterials, ACS Appl. Mater. Interfaces 9 (2017) 21618–21630, https://doi.org/10.1021/acsami.7b03127.

[21] J. Chen, G. Hu, T. Li, Y. Chen, M. Gao, Q. Li, L. Hao, Y. Jia, L. Wang, Y. Wang, Fusion peptide engineered "statically-versatile" titanium implant simultaneously enhancing anti-infection, vascularization and osseointegration, Biomaterials 264 (2021), 120446, https://doi.org/10.1016/j.biomaterials.2020.120446.

[22] M. Xiang, M. Zhu, Z. Yang, P. He, J. Wei, X. Gao, J. Song, Dual-Functionalized apatite nanocomposites with enhanced cytocompatibility and osteogenesis for periodontal bone regeneration, ACS Biomater. Sci. Eng. 6 (2020) 1704–1714, https://doi.org/10.1021/acsbiomaterials.9b01893.

[23] J. Wu, Y. Liu, Q. Cao, T. Yu, J. Zhang, Q. Liu, X. Yang, Growth factors enhanced angiogenesis and osteogenesis on polydopamine coated titanium surface for bone regeneration, Mater. Des. 196 (2020), 109162, https://doi.org/10.1016/j.matdes.2020.109162.

[24] J. Li, J. Wei, A. Li, H. Liu, J. Sun, H. Qiao, A dual peptide sustained-release system based on nanohydroxyapatite/polyamide 66 scaffold for synergistic-enhancing diabetic rats' fracture healing in osteogenesis and angiogenesis, Front. Bioeng. Biotechnol. 9 (2021), 657699, https://doi.org/10.3389/fbioe.2021.657699.

[25] K.-f. Ren, M. Hu, H. Zhang, B.-c. Li, W.-x. Lei, J.-y. Chen, H. Chang, L.-m. Wang, J. Ji, Layer-by-layer assembly as a robust method to construct extracellular matrix mimic surfaces to modulate cell behavior, Prog. Polym. Sci. 92 (2019) 1–34, https://doi.org/10.1016/j.progpolymsci.2019.02.004.

[26] G. Sathishkumar, K. Gopinath, K. Zhang, E.-T. Kang, L. Xu, Y. Yu, Recent progress in tannic acid-driven antibacterial/antifouling surface coating strategies, J. Mater. Chem. B 10 (2022) 2296–2315, https://doi.org/10.1039/d1tb02073k.

[27] Y. Cheng, J. Tang, X. He, G. Sathishkumar, Y. Wang, K. Zhang, X. Rao, E.T. Kang, L. Q. Xu, Tannic acid-promoted deposition of glucose oxidase on titanium surfaces for mitigation of persistent bacterial infections, Adv. Mater. Interfac. 9 (2022), 2201506, https://doi.org/10.1002/admi.202201506.

[28] Y. Han, R.P.M. Lafleur, J. Zhou, W. Xu, Z. Lin, J.J. Richardson, F. Caruso, Role of molecular interactions in supramolecular polypeptide-polyphenol networks for engineering functional materials, J. Am. Chem. Soc. 144 (2022) 12510–12519, https://doi.org/10.1021/jacs.2c05052.

[29] L.Q. Xu, K.-G. Neoh, E.-T. Kang, Natural polyphenols as versatile platforms for material engineering and surface functionalization, Prog. Polym. Sci. 87 (2018) 165–196, https://doi.org/10.1016/j.progpolymsci.2018.08.005.

[30] F. Höök, J. Vörös, M. Rodahl, R. Kurrat, P. Böni, J. Ramsden, M. Textor, N. Spencer, P. Tengvall, J. Gold, A comparative study of protein adsorption on titanium oxide surfaces using in situ ellipsometry, optical waveguide lightmode spectroscopy, and quartz crystal microbalance/dissipation, Colloids Surf. B Biointerfaces 24 (2002) 155–170, https://doi.org/10.1016/S0927-7765(01)00236-3.

[31] F. Höök, B. Kasemo, T. Nylander, C. Fant, K. Sott, H. Elwing, Variations in coupled water, viscoelastic properties, and film thickness of a Mefp-1 protein film during adsorption and cross-linking: a quartz crystal microbalance with dissipation monitoring, ellipsometry, and surface plasmon resonance study, Anal. Chem. 73 (2001) 5796–5804, https://doi.org/10.1021/ac0106501.

[32] D. Pang, L. He, L. Wei, H. Zheng, C. Deng, Preparation of a beta-tricalcium phosphate nanocoating and its protein adsorption behaviour by quartz crystal microbalance with dissipation technique, Colloids Surf. B Biointerfaces 162 (2018) 1–7, https://doi.org/10.1016/j.colsurfb.2017.11.020.

[33] R.A. Gittens, L. Scheideler, F. Rupp, S.L. Hyzy, J. Geis-Gerstorfer, Z. Schwartz, B. D. Boyan, A review on the wettability of dental implant surfaces II: biological and clinical aspects, Acta Biomater. 10 (2014) 2907–2918, https://doi.org/10.1016/j.actbio.2014.03.032.

[34] S.C. Sartoretto, A.T. Alves, R.F. Resende, J. Calasans-Maia, J.M. Granjeiro, M. D. Calasans-Maia, Early osseointegration driven by the surface chemistry and wettability of dental implants, J. Appl. Oral Sci. 23 (2015) 279–287, https://doi.org/10.1590/1678-775720140483.

[35] C. Gao, Z. Wang, Z. Jiao, Z. Wu, M. Guo, Y. Wang, J. Liu, P. Zhang, Enhancing antibacterial capability and osseointegration of polyetheretherketone (PEEK) implants by dual-functional surface modification, Mater. Des. 205 (2021), 109733, https://doi.org/10.1016/j.matdes.2021.109733.

[36] A.A. Khalili, M.R. Ahmad, A review of cell adhesion studies for biomedical and biological applications, Int. J. Mol. Sci. 16 (2015) 18149–18184, https://doi.org/10.3390/ijms160818149.

[37] H.C. Blair, Q.C. Larrouture, Y. Li, H. Lin, D. Beer-Stoltz, L. Liu, R.S. Tuan, L. J. Robinson, P.H. Schlesinger, D.J. Nelson, Osteoblast differentiation and bone matrix formation in vivo and in vitro, Tissue Eng., Part B 23 (2017) 268–280, https://doi.org/10.1089/ten.TEB.2016.0454.

[38] M. Lind, E. Eriksen, C. Bünger, Bone morphogenetic protein-2 but not bone morphogenetic protein-4 and-6 stimulates chemotactic migration of human osteoblasts, human marrow osteoblasts, and U2-OS cells, Bone 18 (1996) 53–57, https://doi.org/10.1016/8756-3282(95)00423-8.

[39] S. Jeon, J.H. Lee, H.J. Jang, Y.B. Lee, B. Kim, M.S. Kang, Y.C. Shin, D.M. Shin, S. W. Hong, D.W. Han, Spontaneously promoted osteogenic differentiation of MC3T3-E1 preosteoblasts on ultrathin layers of black phosphorus, Mater. Sci. Eng., C 128 (2021), 112309, https://doi.org/10.1016/j.msec.2021.112309.

[40] H. Sun, J. Xu, Y. Wang, S. Shen, X. Xu, L. Zhang, Q. Jiang, Bone microenvironment regulative hydrogels with ROS scavenging and prolonged oxygen-generating for enhancing bone repair, Bioact. Mater. 24 (2023) 477–496, https://doi.org/10.1016/j.bioactmat.2022.12.021.

[41] L. Malaval, D. Modrowski, A.K. Gupta, J.E. Aubin, Cellular expression of bone-related proteins during in vitro osteogenesis in rat bone marrow stromal cell cultures, J. Cell. Physiol. 158 (1994) 555–572, https://doi.org/10.1002/jcp.1041580322.

[42] T.R. Kuo, C.H. Chen, Bone biomarker for the clinical assessment of osteoporosis: recent developments and future perspectives, Biomark. Res. 5 (2017), https://doi.org/10.1186/s40364-017-0097-4.
[43] Y. Zuo, Q. Xiong, Q. Li, B. Zhao, F. Xue, L. Shen, H. Li, Q. Yuan, S. Cao, Osteogenic growth peptide (OGP)-loaded amphiphilic peptide (NapFFY) supramolecular hydrogel promotes osteogenesis and bone tissue reconstruction, Int. J. Biol. Macromol. 195 (2022) 558–564, https://doi.org/10.1016/j.ijbiomac.2021.12.028.
[44] J. An, H. Yang, Q. Zhang, C. Liu, J. Zhao, L. Zhang, B. Chen, Natural products for treatment of osteoporosis: the effects and mechanisms on promoting osteoblast-mediated bone formation, Life Sci. 147 (2016) 46–58, https://doi.org/10.1016/j.lfs.2016.01.024.
[45] S. Xiao, J. Wei, S. Jin, X. Xia, L. Yuan, Q. Zou, Y. Zuo, J. Li, Y. Li, A multifunctional coating strategy for promotion of immunomodulatory and osteo/angio-genic activity, Adv. Funct. Mater. 33 (2023), 2208968, https://doi.org/10.1002/adfm.202208968.
[46] T.T. Nguyen, Y.S. Jang, Y.K. Kim, S.Y. Kim, M.H. Lee, T.S. Bae, Osteogenesis-related gene expression and guided bone regeneration of a strontium-doped calcium-phosphate-coated titanium mesh, ACS Biomater. Sci. Eng. 5 (2019) 6715–6724, https://doi.org/10.1021/acsbiomaterials.9b01042.
[47] Y. Zhu, D. Zhou, X. Zan, Q. Ye, S. Sheng, Engineering the surfaces of orthopedic implants with osteogenesis and antioxidants to enhance bone formation in vitro and in vivo, Colloids Surf. B Biointerfaces 212 (2022), 112319, https://doi.org/10.1016/j.colsurfb.2022.112319.